

1 Modeling tabular icebergs coupled to an ocean model

2 **A. A. Stern¹, A. Adcroft¹, O. Sergienko¹, G. Marques¹, R. Hallberg¹**

3 ¹Geophysical Fluid Dynamics Laboratory, Princeton University

4 ¹201 Forrestal Rd, Princeton, NJ 08540, USA

5 **Key Points:**

- 6 • = enter point 1 here =
7 • = enter point 2 here =
8 • = enter point 3 here =

9 **Abstract**

10 The calving of large tabular icebergs from the Antarctic ice shelves accounts for approximately half of Antarctic ice-shelf decay. After calving, these tabular icebergs drift across
 11 large distances, altering regional ocean circulation, bottom-water formation, sea-ice production
 12 and biological primary productivity in the icebergs' vicinity. However, despite
 13 their importance, the current generation of numerical models is unable to represent large
 14 tabular icebergs in a physically realistic way. In this study we develop a novel framework
 15 to model large tabular icebergs submerged in the ocean. In this framework, tabular ice-
 16 bergs are constructed out of Lagrangian elements that drift in the ocean, and are held to-
 17 gether by numerical bonds. By breaking these bonds, a tabular iceberg can be made to
 18 split into smaller pieces, or to break away from an ice shelf. We describe the Lagrangian
 19 bonded iceberg model and discuss a number of the technical elements involved in its de-
 20 velopment. We demonstrate the capabilities of the model by modeling a tabular iceberg
 21 drifting away an idealized ice shelf.

23 **1 Introduction**

24 The Antarctic ice shelves are characterized by large infrequent calving events where
 25 massive pieces of the ice shelves break off, to create large tabular icebergs. Observational
 26 estimates suggest that over the past 30 years approximately half of Antarctic ice-shelf de-
 27 cay is due to iceberg calving, while the other half occurs through ice-shelf melting [De-
 28 poorter et al , 2013; Rignot et al , 2013]. Iceberg sizes appear to fit a power law distri-
 29 bution, with the majority of icebergs being small ($L < 1 \text{ km}$), while the far less numerous
 30 large tabular icebergs ($L > 5 \text{ km}$) account for more than 90% of the icebergs mass [Tour-
 31 nadre et al , 2016].

32 After calving, icebergs slowly drift away from their source glaciers, often becom-
 33 ing stuck in sea ice, or grounding along the Antarctic coast [Lichey and Hellmer , 2001;
 34 Dowdeswell and Bamber , 2007]. Large tabular icebergs extend deep into the water col-
 35 umn, and have the potential to disrupt ocean circulation patterns for months or even years
 36 after calving [Robinson et al , 2012; Stern et al , 2015]. The freshwater flux from iceberg
 37 melt impacts ocean hydrography around the iceberg, influencing sea-ice production and
 38 bottom-water formation [Arrigo et al , 2002; Robinson et al , 2012; Nicholls et al , 2009;
 39 Fogwill et al , 2016]. The long distances traveled by large icebergs before melting means
 40 that their meltwater impact is often felt hundreds of kilometers away from their calving
 41 origins [Stern et al , 2016]. Meltwater injection (and the accompanying upwelling) from
 42 icebergs can also influence biological productivity by providing nutrients to the surface
 43 ocean or changing sea ice conditions [Arrigo et al , 2002; Vernet et al , 2012; Biddle et
 44 al , 2015]. The increased productivity associated with free-floating tabular icebergs has
 45 been linked with local increases in ocean carbon uptake, potentially large enough to be a
 46 significant fraction of the Southern Ocean carbon sequestration [Smith et al , 2007].

47 In recent years, there has been an increased interest in iceberg drift and decay. This
 48 surge of interest has been driven by (i) the need to understand polar freshwater cycles
 49 in order to create realistic climate forecasts and sea level projections [Silva et al , 2006;
 50 Shepherd and Wingham , 2007; Rignot et al , 2013]; and (ii) the increased use of high-
 51 latitudes iceberg-filled waters for shipping lanes and offshore hydrocarbon exploration
 52 in the Arctic [Pizzolato et al , 2012; Unger , 2014; Henderson and Loe , 2016]. The in-
 53 creased interest in icebergs has led to the development of numerical models of iceberg
 54 drift and decay [Mountain , 1980; Bigg et al , 1997; Gladstone et al , 2001; Kubat et al
 55 , 2005], some of which have been included in global General Circulation Models [Mar-
 56 tin and Adcroft , 2010; Marsh et al , 2015]. These iceberg drift models treat icebergs as
 57 Lagrangian point particles, which are advected by the flow, and melt according to cer-
 58 tain parameterizations for icebergs melt. Since icebergs are treated as point particles, ice-
 59 berg drift models are mostly suitable for modeling icebergs smaller than an ocean grid

60 cell. Consequently, these models have mostly been used to represent icebergs smaller than
 61 3.5 km on a global scale [Jongma et al , 2009; Martin and Adcroft , 2010; Marsh et al ,
 62 2015].

63 Point-particle iceberg drift models are less suitable for modeling larger tabular ice-
 64 bergs, where the size and structure of the iceberg may be an important feature in deter-
 65 mining their drift and decay [Stern et al , 2016]. They also are not suitable for studying
 66 the local effects that icebergs have on the surrounding ocean, or the small scale processes
 67 that influence iceberg melt and decay [Wagner et al , 2014; Stern et al , 2015]. For this
 68 reason, tabular icebergs ($L > 5$ km) are currently not represented in the iceberg drift mod-
 69 els used in climate models, even though observations suggest that tabular icebergs account
 70 for the vast majority of the total Southern Hemisphere iceberg mass [Tournadre et al ,
 71 2016].

72 The goal of this study is to develop a new iceberg model where tabular icebergs are
 73 explicitly resolved. In this model, icebergs are no longer treated as point particles that in-
 74 teract with the ocean at a single location, but rather icebergs are given structure, so that
 75 they interact with the ocean across multiple ocean grid cells and depress the ocean surface
 76 over a wide area. To do this, we create tabular icebergs out of many Lagrangian elements
 77 with finite extent which are ‘bonded’ together by numerical bonds. The numerical bonds
 78 hold the ice elements together and allow a collection of elements to move as a unit (see
 79 schematic in Figure 1). By manually breaking these bonds, we can simulate iceberg calv-
 80 ing, allowing us to study the ocean response to a large tabular iceberg detaching from an
 81 ice shelf (e.g.: Figure 2 and 3) or the fracturing of a large iceberg into smaller pieces.

82 The Lagrangian model developed in this study is referred to at the Lagrangian Bonded
 83 Iceberg Model (LBIM). Section 2 gives a description of many of the key aspects of the
 84 LBIM. Since this model is a new approach to modeling icebergs, we present many of the
 85 technical elements involved in constructing the model. In section 3 and 4, we demonstrate
 86 the capabilities of the model by simulating a tabular iceberg detaching from an idealized
 87 ice shelf.

88 2 Model description

89 The LBIM is a Lagrangian particle-based model (or discrete element model) in that
 90 the objects of the model are Lagrangian elements. Each element represents a mass of ice
 91 that is floating in the ocean, and has a position, velocity, mass, and a set of dimensions,
 92 which can evolve in time. The motion of each element is determined by a momentum
 93 equation which is solved in the (Lagrangian) reference frame of the element. The ele-
 94 ments are forced by oceanic and atmospheric forces, which are provided by the user, or
 95 are determined by coupling the LBIM to an ocean/atmosphere model. The elements also
 96 interact with one another and can be bonded together to form larger structures. The an-
 97 gular momentum of the elements is not modeled explicitly; instead rotational motion of
 98 larger structures emerge as a consequence of bond orientation and collective motion. In
 99 different contexts, the LBIM elements can be thought to represent individual icebergs, sea
 100 ice flows, or, when the elements are bonded together, they can represent larger structures
 101 such as tabular icebergs or ice shelves.

102 The LBIM is developed on the code base of an existing iceberg drift model [Martin
 103 and Adcroft , 2010; Stern et al , 2016]. When run with the correct set of runtime flags,
 104 the model runs as a traditional iceberg drift model.

105 2.1 Equations of motion

106 The elements drift in the ocean, forced by atmosphere, ocean and sea-ice drag forces,
 107 as well as the Coriolis force and a force due to the sea surface slope. When these ice el-

ements move alone (without interactions with other elements), they can be thought of as representing individual (or clusters of) small icebergs, and follow the same equations described in the iceberg drift model of Martin and Adcroft [2010] (based on the equations outlined in Bigg et al [1997] and Gladstone et al [2001]).

In addition to the environmental forces, the elements in the LBIM experience interactive forces due to the presence of other elements. Two types of interactive forces are included between elements. The first force is a repulsive force which is applied to elements to prevent them from moving too close to one another. This repulsive force prevents icebergs from piling up on top of one another. The second interactive force is a force due to numerical ‘bonds’, and is only applied if two elements are labelled as ‘bonded’. When two elements are bonded, each element feels an attractive force that prevents the elements from moving too far apart from one another. The interactive forces between two bonded elements are defined such that in the absence of other forces the elements come to rest adjacent to one another, with no overlap of the iceberg areas.

The momentum equation for each element is given by

$$M \frac{D\vec{u}}{Dt} = \vec{F}_A + \vec{F}_W + \vec{F}_R + \vec{F}_C + \vec{F}_{SS} + \vec{F}_{SI} + \vec{F}_{IA}, \quad (1)$$

where $\frac{D}{Dt}$ is the total (Lagrangian) derivative, M is the mass of the element, \vec{u} is the velocity of the element, and the terms on the right hand side give the forces on the element due to air drag (\vec{F}_A), water drag (\vec{F}_W), sea ice drag (\vec{F}_{SI}), Coriolis force (\vec{F}_C), wave radiation force (\vec{F}_R), sea surface slope (\vec{F}_{SS}), and interactions with other elements (\vec{F}_{IA}). The environmental forces are the same as those presented in Martin and Adcroft [2010], and are provided for completeness in Appendix A. The details of the interactive forces are provided in below.

2.2 Interactive Forces

The interactive force on an element is calculated by adding together the interactions with all other elements, such that the interactive force on element i , $(\vec{F}_{IA})_i$ is given by:

$$(\vec{F}_{IA})_i = \sum_{j \neq i} (\vec{F}_{IA})_{ij}, \quad (2)$$

where $(\vec{F}_{IA})_{ij}$ is the force on element i by element j . Both bonded and repulsive interactions are modeled using elastic stresses with frictional damping. The elastic component of the force is a function of the distance between the two elements, while the frictional damping force depends on the relative velocity of the two elements.

To describe the forces between two elements, we begin by introducing some notation. Let \vec{x}_i , \vec{x}_j be the positions of elements i and j . The distance between elements i and j is

$$d_{ij} = |\vec{x}_i - \vec{x}_j|. \quad (3)$$

When calculating the interactive forces between elements, the elements are assumed to be circular. We define the interaction diameter of an element by

$$D_i = 2 \sqrt{\frac{A_i}{\pi}}, \quad (4)$$

where A_i is the planar surface area of element i . Using this, we define the critical interactive length scale,

$$L_{ij} = \frac{D_i + D_j}{2}, \quad (5)$$

which governs interactions between elements i and j . Repulsive forces are only applied when $d_{i,j} < L_{i,j}$, while for $d_{i,j} > L_{i,j}$ attractive bonded forces are applied when a bond exists between element i and j . Bond and repulsive forces are designed such that in the

absence of other forces, bonded particles will settle in an equilibrium position where elements are separated by the critical interaction length scale $L_{i,j}$.

To aid in notation, we define a bond matrix B_{ij} such that $B_{ij} = 1$ if elements i and j are bonded together and $B_{ij} = 0$ otherwise. Using this notation, the interactive force $(\vec{F}_{IA})_{ij}$ on an element i by an element j is given by

$$(\vec{F}_{IA})_{ij} = \begin{cases} (\vec{F}_e)_{ij} + (\vec{F}_d)_{ij} & \text{if } d_{ij} \leq L_{ij} \\ (\vec{F}_e)_{ij} + (\vec{F}_d)_{ij} & \text{if } d_{ij} > L_{ij} \text{ and } B_{ij} = 1 \\ 0 & \text{if } d_{ij} > L_{ij} \text{ and } B_{ij} = 0 \end{cases} \quad (6)$$

$(\vec{F}_e)_{ij}$ and $(\vec{F}_d)_{ij}$ are the elastic and frictional damping components of the interactive force between elements i and j. The elastic force $(\vec{F}_e)_{ij}$ between elements is given by

$$(\vec{F}_e)_{ij} = -\kappa_e (d_{i,j} - L_{i,j}) T_{i,j} \vec{r}_{ij}, \quad (7)$$

where $\vec{r}_{ij} = \frac{(\vec{x}_i - \vec{x}_j)}{|\vec{x}_i - \vec{x}_j|}$ is the directional unit vector between the position of element i and j, κ_e is the spring constant, and $T_{i,j}$ is the minimum of the thickness of elements i, j. The interactive forces obey Newton's 3rd Law (i.e.: $(\vec{F}_{IA})_{ij} = -(\vec{F}_{IA})_{ji}$). The minimum thickness, $T_{i,j}$, is preferred to the average thickness, since this means that for two bonded elements a fixed distance apart, the acceleration due to elastic forces is bounded, even when the thickness of one of the elements approaches zero.

The frictional damping force has components that damp both the relative radial velocity and relative transverse velocities of the two elements. If \vec{r}_{ij}^\perp is the direction vector perpendicular to \vec{r}_{ij} , and $P_{\vec{r}_{ij}}$ and $P_{\vec{r}_{ij}^\perp}$ are the projection matrices that project onto \vec{r}_{ij} and \vec{r}_{ij}^\perp respectively, then the frictional damping force is given by

$$(\vec{F}_d)_{ij} = \left(-c_r P_{\vec{r}_{ij}} - c_t P_{\vec{r}_{ij}^\perp} \right) \cdot (\vec{u}_i - \vec{u}_j) \quad (8)$$

Here c_r and c_t are the radial and transverse drag coefficients. For the simulation below, we set $c_r = 2\sqrt{\kappa_e}$ and $c_t = \frac{1}{4}c_r$ so that the radial elastic force is critically damped, and the transverse damping is sub critical. The damping forces are implemented using an implicit time stepping scheme, to avoid stability issues for very small elements (details found in Appendix B).

The effectiveness of the repulsive forces can be seen in Figure 4, which shows an uncoupled (ice only) simulation where ice elements drift westward into a bay, and eventually come to rest with minimal overlap between elements. The effectiveness of the numerical bonds is demonstrated in Figure 5, where tabular icebergs (constructed from many ice elements bonded together) and individual icebergs (unbonded elements) drift together towards a convex coast line. When the tabular icebergs arrive at the coast, they bump into the coastline and begin to rotate, influencing the paths of the other icebergs. In this example we see that modeling large structures using small elements bonded together, allows us to achieve large-scale structure and rotational motion, without having to include an equation for the angular momentum of the elements (as discussed in Jakobsen [2001]). Animations of these uncoupled simulations can be found in the supplementary materials.

2.3 Initializing element geometry and packing

For purposes of packing, we assume that elements have surface areas which are shaped as equally-sized regular hexagons (note that the elements are assumed to be circular for purposes of interactions, but are assumed to be hexagonal for packing purposes). When packing these elements together, the hexagonal elements are initially arranged in a staggered lattice, with each element bonded to the adjacent elements (see Figure 1). In this arrangement, each element (away from the edges) is bonded to six other elements.

187 The bonds between elements form a pattern of equilateral triangles, which give the larger
 188 structure rigidity. The circular shape of elements (used for interactions) is inscribed within
 189 the hexagonal shape used for packing (Figure 1). The centers of adjacent elements are ini-
 190 tially separated by a distance $d_{i,j} = L_{i,j} = 2A_p$, where A_p is the length the apothems of
 191 the hexagons.

192 Some experiments were also performed using rectangular elements, arranged in a a
 193 regular (non-staggered) lattice. In this case, each element forms four bonds with adjacent
 194 elements. However, the resultant structures were found to be much less rigid and tended
 195 to collapse when sufficient forces was applied. For this reason, hexagonal elements are
 196 used here.

197 2.4 Ocean-ice and ice-ocean coupling

198 The LBIM is coupled to the ocean model via a two-way synchronous coupling,
 199 meaning that ocean-model fields are passed to the LBIM, and the LBIM fields are passed
 200 back to the ocean model at every time step. Passing fields between the two models in-
 201 volves interpolating the fields from the ocean model's Eulerian grid onto the LBIM's 'La-
 202 grangian grid' (i.e.: onto the ice elements, Figure 1), and aggregating fields from the La-
 203 grangian elements onto the ocean-model's Eulerian grid.

204 The coupling from the ocean model to the LBIM is straight forward: at every time
 205 step, the ocean mixed layer temperature, salinity, velocity and sea-ice concentration are
 206 passed from the ocean model to the LBIM, to be used in the momentum and thermo-
 207 dynamic equations of the ice elements. Since tabular icebergs are explicitly resolved in
 208 the ocean, it is sufficient for each element to interact with ocean mixed layer only (i.e.:
 209 there is no need to manually embed icebergs into the ocean by integrating ocean fields
 210 over the icebergs' thickness, as suggested in Merino et al [2016]). Within the LBIM, the
 211 ocean model fields are interpolated onto the Lagrangian grid using a bilinear interpolation
 212 scheme.

213 The coupling from the LBIM to ocean model is more complex. The LBIM influ-
 214 ences the ocean by: (i) applying a pressure to the ocean surface, (ii) imposing heat, salt
 215 and mass fluxes on the ocean, associated with ice melting, and (iii) affecting the upper
 216 ocean by applying a no-slip boundary condition and frictional velocity beneath the ice.
 217 Fields from the LBIM are aggregated from the Lagrangian elements to the Eulerian ocean
 218 grid before they are passed to the ocean model. Since LBIM applies large pressures to
 219 the ocean surface, sudden changes to the aggregated pressure field pressure can trigger
 220 tsunamis within the ocean model, making the ocean model unrealistic. The aggregation
 221 scheme is therefore designed such that there are no jumps in pressure as an element moves
 222 from one grid cell to the next, and total pressure is conserved as an element moves.

223 The aggregation of the LBIM fields onto the ocean grid is done in a way that is
 224 consistent with the shape of the elements in the LBIM (see Section 2.3). Fields are 'spread'
 225 to the ocean model grid by exactly calculating what fraction of an element's surface area
 226 lies in a particular grid box, and dividing the field in proportion to this fraction. For ex-
 227 ample, consider a hexagonal element in the LBIM, which is positioned such that it inter-
 228 sects four ocean grid cells (inset panel in Figure 1). In this situation, the mass of the ele-
 229 ment is divided between these four ocean cells in proportion to the overlap area between
 230 the hexagonal element and the grid cell (this fraction is shown by the colors in the inset
 231 panel in Figure 1). An advantage of this approach is that there are no jumps in pressure as
 232 an element moves from one grid cell to another.

233 The numerical calculation of the intersection between hexagons and the ocean grid
 234 is simplified by dividing the hexagon into 6 equilateral triangles. This method allows for
 235 the intersection to be found even when the hexagon is not aligned with the grid.

236 The aggregation scheme is coded with the restriction that an element's area can only
 237 intersect a maximum of four ocean grid cells at a time. A consequence of this is that this
 238 sets a limit on the maximum size of elements that can be represented using this model,
 239 i.e.: the longest horizontal dimension of an ice element must be smaller than the ocean
 240 grid spacing. Larger ice structures are constructed by bonding together smaller elements.

241 2.5 Thermodynamics

242 The ice elements decay according to a number of melt parameterizations. As the
 243 ice elements melt, their mass decreases, and the appropriate salt, mass and heat fluxes are
 244 passed to the ocean. In this section we described the melt parametrization for bonded,
 245 unbonded and partially bonded elements.

246 As mentioned above, ice elements which do not interact with other elements are
 247 modeled identically to the point particle icebergs described in Martin and Adcroft [2010].
 248 These elements melt according to three semi-empirical parametrization for melt commonly
 249 used in previous iceberg studies [Gladstone et al , 2001; Martin and Adcroft , 2010].
 250 Three types of iceberg melting are used: basal melt, M_b , melt due to wave erosion, M_e
 251 and melt due to buoyant convection, M_v . M_e and M_v are applied to the sides of the ice
 252 element, while M_b is applied at the ice element base. The details of M_b . M_v and M_e are
 253 given in Appendix A.

254 When multiple elements are bonded together to form larger structures, it is no longer
 255 appropriate to use the parameterizations for melt developed for individual point-particle
 256 icebergs. An element which is completely surrounded by other elements, is meant to rep-
 257 resent a piece of ice in the middle of a large structure, and hence will not experience a
 258 melt at its sides due to wave erosion or buoyant convection. Also, the iceberg basal melt
 259 rate, M_b described above is based on boundary layer theory of flow past a finite plate, and
 260 is only appropriate for basal surfaces where the distance from the leading edge is suffi-
 261 ciently small [Eckert , 1950; Weeks and Campbell , 1973]. For an element in the interior
 262 of large structures, the distance from the edge of the structure is large, and so using M_b
 263 for the basal melt is not appropriate. Instead, the basal melt, M_s is determined using the
 264 three equation model for basal melt, which is a typical melting parametrization beneath
 265 used beneath ice shelves [Holland and Jenkins , 1999].

266 When using both individual elements and bonded elements in the same simulation,
 267 we determine which melt rate parameterizations to use based on the amount of bonds
 268 that each element has. An element which is in the center of a large structure will form
 269 the maximum number of bonds, while unbonded elements form zero bonds. If maximum
 270 number of bonds that an element can form (given the shape of the element) is N_{max} , and
 271 the number bonds that an element has is N_b , then the side melt and bottom melt for that
 272 element are given by

$$M_{side} = \frac{(N_{max} - N_b)}{N_{max}} (M_v + M_e) \quad (9)$$

273 and

$$M_{bottom} = \frac{(N_{max} - N_b)}{N_{max}} M_b + \frac{N_b}{N_{max}} M_s \quad (10)$$

274 respectively. In this way, elements with no bonds, melt like point-particle icebergs, ele-
 275 ments at the center of large structures melt like ice shelves, and elements at the sides of
 276 large structures have a combination of iceberg side and basal melt, and ice-shelf melt.

277 2.6 Algorithms and computational efficiency

278 Including interactions between elements leads to an increase in the computational
 279 complexity of the model. In this subsection we comment on some of the algorithmic pro-
 280 cedures that have been used to increase the computational efficiency.

281 **2.6.1 Interactions and Bonds**

282 At every time step, we calculate the force on each element due to interactions with
 283 every other element. In principle, this involves order N^2 operations (for N elements).
 284 However, since each element only has repulsive interactions with elements that are less
 285 than one ocean grid cell away, and each element only has bonded interactions with a
 286 small number of other elements, we are able to reduce the complexity of the system.

287 The complexity reduction is achieved by storing the element data in an efficient way
 288 that prevents having to search through all element pairs to check if they are close to one
 289 another or are bonded with one another. The data storage system works as follows: pointers
 290 to the memory structures containing each element are stored in linked list data struc-
 291 tures, which allow elements to be added and removed from the lists easily without re-
 292 structuring the entire list. Instead of using one list for all the elements on a processor (as
 293 was done in the original code [Martin and Adcroft , 2010]), we use a separate linked list
 294 for each ocean grid cell. When an element moves between ocean grid cells, it is removed
 295 from its original list and added to the list corresponding to its new ocean grid cell. Since
 296 the area of elements has to be smaller than the area of an ocean grid cell, the critical in-
 297 teraction length scale (equation 5) is less than the length of a grid cell. This means that
 298 elements only experience repulsive forces with other elements in the same ocean grid cell,
 299 or in one of the 8 adjacent cells. At each time step and for each element i , the code tra-
 300 verses these linked lists of the 9 surrounding grid cells, and applies a repulsive force if
 301 $d_{i,j} < L_{ij}$ (whether the elements are bonded or not). Limiting the possible repulsive in-
 302 teractions to elements in these 9 linked lists substantially reduces the computational time
 303 needed to calculate the total interactive forces.

304 The attractive part of the bonded interactions are handled separately. Each bond is
 305 assigned a piece of memory. Each ice element contains a linked list of each of its bonds
 306 (typically up to six bonds per element). At every time step, the code traverses the lists
 307 of bonded elements, and adds an attractive bonded force corresponding to these bonds if
 308 $d_{i,j} > L_{ij}$. (the repulsive bonded force to be applied when $d_{i,j} < L_{ij}$ is already accounted
 309 for by the procedure outlined in the previous paragraph). Having a list of bonds stored
 310 with each element reduces the computational complexity of bonded interactions from
 311 order N^2 to order N. Handling bonded attractive forces separately to the repulsive and
 312 non-bonded forces means that we do not need to check whether two elements are bonded,
 313 which further increases the computational efficiency.

314 **2.6.2 Parallelization and halos**

315 The LBIM runs on multiple processors in parallel (using the same grid decomposi-
 316 tion as the ocean model). When elements move from an ocean cell on one processor to
 317 an ocean cell on a second processor, the memory has to be passed from one processor the
 318 next, added and removed to the appropriate lists and the memory has to be allocated and
 319 deallocated correctly. Element interactions across the edge of processors are handled us-
 320 ing computational halos. A computational halo is a copy of the edge of a one processor
 321 which is appended to the edge of a second processor, so that the first processor can ‘see’
 322 the second processor during a time step. Before each time step, elements at the edges of
 323 each processor are copied onto the halos of adjacent processors so that they can be used
 324 in calculating the interactive forces. After each time step, these halos are removed, and
 325 the process is repeated. These halo updates are one of the most computationally expensive
 326 parts of the LBIM.

327 Keeping track of pairs of bonded elements that move across a processor edge re-
 328 quires a lot of book keeping since bonds have to be severed and reconnected. Details of
 329 how the bonds are broken and reconnected across processor boundaries are provided in
 330 Appendix C.

331 **2.6.3 Time stepping**

332 The ice elements in the LBIM are advected using a semi-implicit velocity Verlet
 333 time-stepping scheme. The velocity Verlet time stepping scheme is commonly used in
 334 DEM models in video games because it is computational efficient and has desirable stabil-
 335 ity properties [Jakobsen , 2001]. This time stepping scheme was preferred to the Runge-
 336 Kutta 4, which was used in the iceberg model of Martin and Adcroft [2010] since the
 337 Verlet time stepping only requires a calculation of the interactive forces once per time step
 338 (while the Runge-Kutta scheme requires the interactive forces to be calculated four times).
 339 Since the calculation of the interactive forces is one of the most computationally expen-
 340 sive part of the algorithm, the Verlet scheme leads to a significant increase in the speed of
 341 the model. We note that the Verlet scheme used in the LBIM contains a modification of
 342 the original (fully explicit) velocity Verlet time stepping scheme in that damping terms are
 343 treated implicitly (which increases the numerical stability). The details of this time step-
 344 ping scheme are outlined in Appendix B.

345 **3 Experiment Setup**

346 The introduction of Lagrangian elements, numerical bonds and interpolation schemes
 347 between the Eulerian and Lagrangian grids (discussed in Section 2) means that we now
 348 have the tools to model large tabular icebergs submerged in the ocean. We demonstrate
 349 this capability by simulating a tabular iceberg drifting away from an idealized ice shelf.

350 **3.1 Model configuration**

351 We initialized our simulation using the experimental setup created for the Marine
 352 Ice Ocean Modeling Inter-comparison Project (MISOMIP) [Asay-Davis et al , 2016]. The
 353 configuration consists of an idealized ice shelf in a rectangular domain. The domain is
 354 $L_x = 80$ km wide and $L_y = 480$ km long, and contains an ice shelf which is grounded on
 355 the south side of the domain and has an ice front at $y=650$ km. The ice thickness and
 356 bottom topography of this setup are shown in Figure 6a and 6b respectively, with the
 357 grounding line position drawn in for reference. The configuration is the same as that of
 358 the Ocean0 setup in the MISOMIP, with a few minor changes to the ice-shelf geometry
 359 (see Supplementary Material for details).

360 **3.2 Initializing Lagrangian elements:**

361 The idealized ice shelf is constructed out of Lagrangian ice elements. Ice elements
 362 are hexagonal and are arranged in a regular staggered lattice (as discussed in Section 2.3).
 363 The sides of the gridded hexagons are initialized with length $S = 0.98$ km. Gaps along
 364 the boundaries are filled in using smaller elements so that the total ice-shelf area is pre-
 365 served. The initial mass of the ice elements is determined by a preprocessing inversion
 366 step, which is the inverse of the ‘mass-spreading’ interpolation procedure discussed in
 367 Section 2.3. The ice draft calculated without mass-spreading aggregation (treating ele-
 368 ments as point masses) contains large grid artifacts (Figures 6c). These grid artifacts are
 369 much reduced after the mass-spreading aggregation is applied (Figure 6b).

370 **3.3 Ocean model setup**

371 The LBIM is coupled to the MOM6 ocean model [Hallberg et al , 2013]. The ocean
 372 model is run using a vertical coordinate system which is a hybrid between a sigma-level
 373 and a z-level coordinate. In particular, model layers bend underneath the ice shelf as they
 374 would in a sigma-coordinate model, but collapse to zero thickness when they intersect
 375 with bottom topography, as they would in a z-level model. The coordinate system was
 376 achieved using ALE regridding-remapping scheme [White et al , 2009]. The model uses a

377 horizontal resolution of 2 km, and 72 vertical layers. All simulations were repeated using
 378 the ocean model configured in isopycnal mode (results were similar and are not presented
 379 here).

380 Ocean parameters are as specified in the MISOMIP configuration [Asay-Davis et
 381 al , 2016], and are shown in Table 1. The simulation is initially at rest, with horizontally
 382 uniform initial ocean temperature and salinity profiles which vary linearly between spec-
 383 ified surface and bottom values: $T_{top} = -1.9^\circ \text{C}$, $T_{bottom} = 1.0^\circ \text{C}$, $S_{top} = 33.8 \text{ psu}$,
 384 $S_{bottom} = 34.7 \text{ psu}$. The maximum ocean depth is $H_{ocean} = 720 \text{ m}$. A sponge layer is
 385 used on the northern boundary, which relaxes back to the initial temperature and salinity
 386 with a relaxation time scale of $T_{sponge} = 0.1 \text{ days}$. Melting is set to zero for ocean cells
 387 where the ocean column thickness is less than 10m to avoid using more energy to melt ice
 388 than is present in the water column.

389 3.4 Spinup and iceberg calving:

390 The model is spun up for 5 years with all ice elements being held stationary. After
 391 spinup, a large tabular iceberg is ‘broken off’ from the ice shelf, and allowed to drift into
 392 the open ocean. This is achieved by allowing all ice elements initially within a 14.4 km
 393 radius of the center of the ice front to move freely while the other ice elements continue
 394 to be held stationary. Ice elements less than 12 km from the center of the ice front, are
 395 bonded together to form a semi-circular tabular iceberg. A ring of elements whose dis-
 396 tance, d , from the ice front center obeys $12 \text{ km} \leq d \leq 14.4 \text{ km}$, are allowed to move
 397 freely, but have all their bonds removed. Elements in this half annulus represent fragments
 398 of the ice shelf which calve into small pieces during a large calving event. Breaking the
 399 bonds of these surrounding elements allows the tabular iceberg to move away from the
 400 ice-shelf cavity more easily.

401 After the spinup period, a wind stress $\vec{\tau} = < \tau_x, \tau_y > = < 0.05, 0.05 > \frac{N}{m^2}$ is applied
 402 to drive the tabular iceberg away from the ice-shelf cavity. Perturbation experiments were
 403 performed using other wind stress values.

404 4 Model Results

405 During spinup, the injection of buoyant meltwater at the base of the ice shelf drives
 406 a clockwise circulation within the domain (not shown). The circulation compares well
 407 with an identical static ice-shelf experiment run using an Eulerian ice shelf model [Gold-
 408 berg et al , 2012] (a detailed comparison of the Lagrangian and Eulerian ice shelf models
 409 is presented in a separate study, and is not shown here).

410 Once spinup is complete, the elements near the ice-shelf front are allowed to move
 411 freely, and the icebergs begin to drift away from the ice shelf (see animations in the sup-
 412 plementary materials). The semi-circular tabular iceberg moves as a cohesive unit due
 413 to the presence of the numerical bonds, while the smaller ice fragments quickly disperse
 414 (Figure 2). The tabular iceberg drifts towards the northward east, driven by the wind and
 415 steered by the Coriolis force.

416 A warming of the surface waters is observed around the tabular iceberg, with the
 417 largest warming occurring at the ice-shelf front and along the tabular iceberg’s rounded
 418 edge (Figure 3). This surface warming is caused by upwelling of the warmer waters from
 419 beneath the ice shelf and iceberg. As the icebergs drifts away from the ice shelf, these
 420 warmer waters remain at the surface, mapping of the wake of the iceberg (Figure 3). The
 421 signature of upwelling water in the wake of a drifting tabular iceberg bears some simi-
 422 larity to satellite observations of streaks of increased ocean color in the wake of tabular
 423 iceberg in the Southern Ocean [Duprat et al , 2016], suggesting that the increased pro-

424 ductivity around icebergs may be driven by upwelling water delivering nutrients to the
 425 surface.

426 The motion of the tabular iceberg disturbs the ocean surface, which drives ocean
 427 velocities through out the water column (Figure 7). The elevated shears around the tabu-
 428 lar iceberg lead to increased vertical mixing in the vicinity of the iceberg, which alters
 429 the stratification of the water column (Figure 8), heating the upper ocean. The increased
 430 ocean velocities and increased surface temperatures cause elevated melt rates at the base
 431 of the ice shelf and iceberg (Figure 9). The largest melt rates are observed at the newly
 432 calved ice-shelf front and on the rounded side of the iceberg (Figure 9a), where the ice-
 433 berg calving has created steep ice cliffs. These sharp ice fronts allow for large ocean
 434 currents (Figure 9c), which drive the elevated melt rates. The elevated melt rates act to
 435 smooth out the ice front over time, making the ice cliff less steep. While this is likely a
 436 real phenomena that could be observed in nature, we should be wary of the modeled ve-
 437 locities at the ice cliffs, since large changes in ice thicknesses are often associated with
 438 numerical pressure gradient errors which can drive spurious motion.

439 As mentioned above, the direction (and speed) of the iceberg drift is largely deter-
 440 mined by the wind speed and direction. Perturbation experiments using different wind
 441 stresses show that for sufficiently large winds, the tabular iceberg drifts to the north east
 442 when $\tau_x > 0$, and to the north west when $\tau_x < 0$ (not shown). For a purely zonal wind
 443 stress with $|\tau_x| \leq 0.01 \frac{N}{m^2}$, the iceberg does not move away from the ice shelf. When the
 444 wind is purely offshore ($\tau_x = 0.0 \frac{N}{m^2}$), a meridional wind stress $\tau_y \geq 0.05 \frac{N}{m^2}$ is needed
 445 to move the tabular iceberg away from the ice shelf. While this result is partly an artifact
 446 of the artificial shape of the calving iceberg, it is also consistent with Bassis and Jacobs
 447 [2013] who noted that calving is a two step process consisting of (i) ice-shelf breaking
 448 and (ii) iceberg detachment. The results here suggest that strong (cross-shore) winds may
 449 be required to drive large tabular icebergs away from their mother glaciers.

450 Finally, we note that the numerical bonds in the LBIM are needed in order to allow
 451 the tabular iceberg to retain its shape. Comparing the iceberg calving simulation with an
 452 identical simulation where all numerical bonds have been removed, shows that in the ab-
 453 sence of the bonds, the ice elements quickly disperse (Figure 10). In this case, the model
 454 behavior is more similar to an ice-shelf disintegration and does not create a cohesive tabu-
 455 lar iceberg. By breaking some (but not all) numerical bonds, we can simulate the frac-
 456 turing of tabular icebergs, allowing tabular icebergs to break into smaller pieces (Figure
 457 ???). The breaking of a tabular iceberg increases decay rate of the iceberg by increasing
 458 the surface area of ice exposed to the ocean. Splitting the tabular iceberg into smaller
 459 fragments also allows the fragments of the iceberg to move more rapidly, and be more
 460 strongly influenced by the wind.

461 5 Summary

462 In this study we present a novel framework for representing tabular icebergs in nu-
 463 matical ocean models. In this framework, large tabular icebergs are constructed from col-
 464 lections of Lagrangian elements that are held together by numerical bonds. Constructing
 465 tabular icebergs out of many independent elements allows the icebergs to interact with
 466 the ocean across a wide area (larger than a grid cell), and behave as if they had a finite
 467 size and structure. This is in contrast to previous representations of icebergs in numerical
 468 models [Jongma et al , 2009; Martin and Adcroft , 2010; Marsh et al , 2015] that repre-
 469 sent icebergs as point particles. Explicitly resolving tabular icebergs in the ocean allows
 470 the icebergs to interact with the ocean in a more realistic way, and allows us to study the
 471 effect that tabular icebergs have on the ocean circulation. Including numerical bonds be-
 472 tween elements allows for the possibility of breaking bonds to simulation iceberg calving
 473 and fracture.

The capabilities of the tabular iceberg model were demonstrated by modeling a tabular iceberg drifting away from an idealized ice shelf (also constructed using Lagrangian elements). The results show that explicitly resolving the iceberg in the ocean allowed for a complex interaction between the tabular iceberg and the surrounding ocean. In our setup, the tabular iceberg is driven away from the ice shelf by ocean currents, wind stress, and the Coriolis force. As the iceberg moves through the water, it disturbs the ocean surface, driving barotropic ocean currents. The motion of the iceberg and melt beneath the iceberg drive upwelling along the sides of the iceberg, which entrains ambient water and causes a warming of the surface ocean in the wake of the iceberg. The changing ocean conditions feed back onto the iceberg, affecting its motion and melt rates. The highest melt rates are observed at edge of the iceberg which has the steepest ice cliff. These have the effect of smoothing out the ice edge over time. Simulations without using numerical bonds showed that these bonds are essential for allowing the iceberg to move as a unit. We also demonstrate that by breaking these numerical bonds we can simulate iceberg fracture, which is important process that increases the rate of iceberg decay.

To our knowledge, the model presented in this study is the first model to explicitly resolve drifting tabular icebergs in an ocean model that can be used for climate. A natural extension of this work is to try to include tabular icebergs into a general circulation model (GCM) used for climate projections. However, before this can be done, there are a number of issues that need to be resolved: firstly, the question of how and when to introduce tabular icebergs into the ocean needs to be addressed. For GCM's with active ice shelves, a calving law is needed to decide when to release the tabular iceberg into the ocean. The question of what calving law to use is a topic of ongoing research [Benn et all , 2007; Alley et al , 2008; Levermann et al , 2012; Bassis and Jacobs , 2013] and is still unresolved. One potential way to temporarily bypass this problem would be to run hind-cast simulations using historically observed calving events. A related issue is the question of how and when to break the bonds within the freely floating icebergs to simulation iceberg breakup. Without a rule for iceberg breakup, the tabular icebergs would likely drift to unrealistically low latitudes. Another challenge will be to develop methods to initialize the size and positions of elements on a spherical grid. This study used a cartesian coordinate system, which allowed us to initialize the ice elements in a regular staggered lattice. A different initialization method will be needed to generalize this initialization procedure to curved coordinates which are needed for large scale global simulations. Further work is also needed to understand (and model) the interactions between tabular icebergs and sea ice, and to parametrize the effects of iceberg grounding, as these interactions play a large role in dictating the trajectories of tabular icebergs. However, despite these remaining challenges, the technical framework described in this article is potentially a using step towards including tabular icebergs in global GCM's, and hence a step towards making more accurate projections of future sea level.

6 Appendix A

6.1 Environmental forces on ice elements

The non-interactive forces on an ice element are as described in [Martin and Adcroft , 2010], and are repeated here for completeness. The forces on an element due to air (a), ocean (o) and sea ice (si) drag are given by

$$(\vec{F}_a) = \rho_a(0.5c_{a,v}WF + c_{a,h}LW)|\vec{u}_a - \vec{u}|(\vec{u}_a - \vec{u}), \quad (11)$$

$$(\vec{F}_o) = \rho_o(0.5c_{o,v}W(D - T_{si})F + c_{o,h}LW)|\vec{u}_o - \vec{u}|(\vec{u}_o - \vec{u}), \quad (12)$$

$$(\vec{F}_{si}) = \rho_{si}(0.5c_{si,v}WT_{si}F + c_{si,h}LW)|\vec{u}_{si} - \vec{u}|(\vec{u}_{si} - \vec{u}). \quad (13)$$

Here ρ_a , ρ_o , ρ_{si} , are the density of air, ocean and sea ice, respectively. $c_{a,v}$, $c_{o,v}$ and $c_{si,v}$ are the vertical drag coefficients with air, ocean and sea ice, while $c_{a,h}$, $c_{o,h}$ and $c_{si,h}$ are the respective horizontal drag coefficients. \vec{u}_a , \vec{u}_o , \vec{u}_{si} , are the velocities air,

523 ocean and sea ice, respectively. L, W, T, F and D are the length, width, thickness, free-
 524 board and draft of the ice element. The element thickness is related to the draft and free-
 525 board by $T = F + D$ and $D = \frac{\rho}{\rho_o}T$, where ρ is the ice element density. T_{si} is the sea ice
 526 thickness.

527 The wave radiation force (\vec{F}_R) is given by

$$\vec{F}_R = \frac{1}{2}\rho_o c_r g a \min(a, F) 2 \frac{WL}{W+L} \frac{\vec{v}_a}{|\vec{v}_a|} \quad (14)$$

528 where g is the acceleration due to gravity, a is the wave amplitude empirically related to
 529 the wind speed by $a = 0.010125|\vec{v}_a - \vec{v}_o|$, and c_{wd} is the wave drag coefficient defined as

$$c_{wd} = 0.06 \min\left(\max\left[0, \frac{L - L_c}{L_t - L_c}\right], 1\right), \quad (15)$$

530 where $L_w = 0.32|\vec{v}_a - \vec{v}_o|^2$ is an empirical wave length, $L_c = 0.125L_w$ is the cutoff length,
 531 and $L_t = 0.25L_w$ is the upper limit.

532 The pressure gradient force is approximated as a force due to sea surface slope and
 533 given by

$$\vec{F}_{SS} = -Mg\vec{\nabla}\eta \quad (16)$$

534 where η is the sea surface height.

535 6.2 Melt rate parametrization

536 As discussed in Section 2.5, unbounded ice elements in the LBIM decay according
 537 to parameterizations for iceberg decay typically used in iceberg drift models [Martin and
 538 Adcroft , 2010], while ice elements within larger ice structures have only a basal melt
 539 given by the three equation model [Holland and Jenkins , 1999] .

540 For unbonded ice elements, the element thickness decays due to basal melt at a rate
 541 M_b , while the length and width of the elements decay as a result of melt due to wave ero-
 542 sion, M_e , and melt due to buoyant convection, M_v . Following Gladstone et al [2001] and
 543 Martin and Adcroft [2010], the basal melt rate, wave erosion melt rate, and buoyant con-
 544 vection melt rate are parameterized by

$$M_b = 0.58|\vec{v} - \vec{v}_0|^{0.8} \frac{\tilde{T}_0 - \tilde{T}}{L^{0.2}} \quad (17)$$

$$M_e = \frac{1}{12}S_s \left(1 + \cos[\pi A_i^3]\right) \left(\tilde{T}_0 + 2\right), \quad (18)$$

$$M_v = \left(7.62 \times 10^{-3}\right)\tilde{T}_0 + \left(1.29 \times 10^{-3}\right)\tilde{T}_0^2. \quad (19)$$

547 \tilde{T} is the effective iceberg temperature and is set to $\tilde{T} = 4^\circ\text{C}$, \tilde{T}_0 is the temperature at the
 548 top of the ocean, A_i is the sea ice area fraction, and S_s is the sea state, which is given by
 549 the Beaufort scale

$$S_s = \frac{2}{3}|\vec{u}_a - \vec{u}_o|^{\frac{1}{2}} + \frac{1}{10}|\vec{u}_a - \vec{u}_o| \quad (20)$$

550 All three melt rates are in units of meters per day.

551 For elements inside larger structures, the melt due to wave erosion and melt due to
 552 buoyant convection are set to zero, and the basal melt, M_s is given by the standard three
 553 equation model [Holland and Jenkins , 1999].

554 **7 Appendix B**

555 **7.1 Modified Verlet Algorithm**

556 The LBIM uses a version velocity Verlet time-stepping algorithm, which has been
 557 modified to allow part of the forcing to be calculated implicitly. The traditional velocity
 558 Verlet algorithm is commonly used in molecular dynamics, as it is simple to implement,
 559 second order accurate and computationally efficient [Swope et al , 1982; Omelyan et al ,
 560 2002]. Here we modify the traditional scheme to allow for the drag forces to be modeled
 561 implicitly, which prevents large accelerations for element's whose mass approaches zero.
 562 To do this, we include both an implicit and explicit acceleration, $a = a^{exp} + a^{imp}$. The
 563 explicit acceleration, a^{exp} includes all forcing terms which depend only on the previous
 564 time step and the current position, while the implicit acceleration, a^{imp} includes forcing
 565 terms which depend on the velocity at the current time step (in particular the drag and
 566 Coriolis forces).

567 Using a time step of Δt , and subscripts to denote the time step (so that $t_{n+1} = t_n +$
 568 Δt), the modified velocity Verlet scheme can be written as:

569 1) $x_{n+1} = x_n + u_n \Delta t + \frac{1}{2} \Delta t^2 \left(a_n^{exp} + a_n^{imp} \right).$

570 2) Calculate a_{n+1}^{exp}

571 3) Calculate a_{n+1}^{imp} and $u_{n+1} = u_n + \frac{\Delta t}{2} \left(a_n^{exp} + a_{n+1}^{exp} \right) + (\Delta t) a_{n+1}^{imp}$

572 This scheme reduces to the traditional velocity Verlet when a^{imp} is set to zero.

573 Note that $a_{n+1}^{exp} = a_{n+1}^{exp}(x_{n+1}, t_n)$ is an explicit function of x_{n+1} and other quantities
 574 evaluated at time t_n , while $a_{n+1}^{imp} = a_{n+1}^{imp}(u_{n+1}, x_{n+1}, t_n)$ additionally depends on u_{n+1} ,
 575 and needs to be solved implicitly. For this reason in step three, a_{n+1}^{imp} and u_{n+1} need to be
 576 solved simultaneously, as described in the next subsection.

577 In equation (1), the forces due to ocean drag, atmospheric drag and sea ice drag are
 578 treated implicitly. The force due to sea surface slope and wave radiation are treated ex-
 579 plicitly. The Coriolis term is handled using Crank-Nicolson scheme so that half of the
 580 effect is implicit and half is explicit. The elastic part of the interactive forces is treated ex-
 581 plicitly, while the interactive damping is handled semi-implicitly in that the drag force on
 582 element A by element B depends on the velocities of elements A and B evaluated at time
 583 t_{n+1} and t_n , respectively.

584 **7.2 Solving for the velocity implicitly**

585 Since this modified scheme contains some forcing terms which are handled im-
 586 plicitly, a_{n+1}^{imp} and u_{n+1} need to be calculated simultaneously. We demonstrate how this
 587 is done, using a simplified one-dimensional version of equation (1), neglecting the atmo-
 588 spheric drag, sea ice drag and Coriolis force, so that the only implicitly treated term is the
 589 ocean drag. In this demonstration, we use a superscript to denote the ocean drag force,
 590 F^o , and ocean velocity, u^o , to avoid confusion with the subscripts indicating time step.
 591 We also define an explicit force, F^{exp} , which accounts for all forces not proportional the
 592 element velocity. With these simplifications, the implicit and explicit accelerations are

593
$$a^{exp} = \frac{1}{M} (\vec{F}^{exp}) \quad (21)$$

$$a^{imp} = \frac{1}{M} (F^o) \quad (22)$$

594 The ocean drag force at time t_{n+1} is modeled (mostly) implicitly as

$$F_{n+1}^o = \tilde{c}^o |u_n^o - u_n| (u_n^o - u_{n+1}), \quad (23)$$

595 where \tilde{c}^o is the effective drag coefficient, accounting for the dimensions of the ice element
 596 (see equation 12).

597 Step 3 of the modified velocity Verlet scheme can be rewritten by introducing an
 598 intermediate velocity u^* , which only depends on the velocity and acceleration at time t_n ,

$$u_n^* = u_n + \frac{1}{2}(\Delta t)a_n^{exp}. \quad (24)$$

599 Using this, the updated velocity (Step 3) can be written

$$u_{n+1} = u_n^* + \frac{\Delta t}{2}a_{n+1}^{exp} + (\Delta t)a_{n+1}^{imp}. \quad (25)$$

600 Including the forcing terms into this equations gives

$$u_{n+1} = u_n^* + \frac{\Delta t}{2M}(F_{n+1}^{exp}) + \frac{\Delta t}{M}\left(c_w|u_n^o - u_n|(u_n^o - u_{n+1})\right) \quad (26)$$

601 Solving for $u(t_{n+1})$ in terms of quantities which only depend on the previous time step
 602 gives

$$u_{n+1} = \frac{u_n^* + \frac{\Delta t}{2M}(F_{n+1}^{exp}) + \frac{\Delta t}{M}\left(c_w|u_n^o - u_n|(u_n^o - u_{n+1})\right)}{\left(1 + \frac{\Delta t}{M}c_w|u_n^o - u_n|\right)} \quad (27)$$

603 Once the u_{n+1} has been found, it can be used to calculate the explicit and implicit acceler-
 604 ations, which are required for the next time step.

605 Finally, we note that the the drag term (equation 23) is not entirely implicit, since
 606 the element velocity inside the absolute value is evaluated at time t_n , rather than at time
 607 t_{n+1} . This is done so that we can solve for the updated velocity analytically. One conse-
 608 quence of this is that it can give rise to a small oscillation in the element velocity. This
 609 oscillation is addressed by using a predictive corrective scheme: after solving for a first
 610 guess of the velocity at time t_{n+1} , this estimate of the velocity is used to update the esti-
 611 mate of the drag force (i.e.: inside the absolute value signs). This updated drag, can now
 612 be used to repeat the process described above to find an improved estimate of the velocity.
 613 We found that two iterations were sufficient to remove the unwanted oscillation.

614 The procedure described in this section is easily extended to include more forcing
 615 terms and two dimensions (where it involves inverting a 2×2 matrix).

616 8 Appendix C

617 Connecting bonds across processor boundaries

618 Since the LBIM is parallelized across multiple processors, it often happens that two
 619 elements on different processes are bonded together. Keeping track of numerical bonds
 620 across processor boundaries requires a lot of book keeping. In this section we describe the
 621 how LBIM handles bonds across processor boundaries.

622 The basics of the bond bookkeeping work as follows: consider an element A and
 623 an element B that are bonded together. Each element has a copy of the bond (a piece of
 624 memory which describes the bond between the two elements), which is stored with the
 625 element. Let A-B be the bond stored by element A, and B-A be the bond stored by ele-
 626 ment B. Bond A-B contains a pointer which points to element B and bond B-A contains a
 627 pointer which points to element A.

628 Consider a situation where element A and B are originally on Processor 1, and then
 629 element B moves to Processor 2. When this occurs, the memory assigned to element B
 630 on processor 1 is removed, and is allocated on Processor 2. This means that the pointer
 631 to element B in bond A-B (stored in element A on Processor 1) is no longer assigned.
 632 Similarly, the pointer to element A in bond B-A (stored in element B on Processor 2) is

no longer assigned. Before the next time step, a halo update occurs, so that there is a copy of element A in the halo of Processor 2 and a copy of element B in the halo of Processor 1. After the halo update, the bonds A-B and B-A have to be reconnected on both Processor 1 and 2. To aid in reconnecting the bonds, a copy of the grid cell number of element B is stored in the bond A-B and a copy of the grid cell number of element A is stored in the bond B-A. We refer to this as the ‘most recent address’. Before a bond is moved from one processor to another, the ‘most recent address’ is updated, so that the bond can be reconnected later. To reconnect bond A-B on Processor 1 (for example), we find the most recent address of element B, and search through the list of elements in the grid cell corresponding to the most recent address of element B until element B is found. The pointer to element B in bond A-B is reassigned, and the bond is said to be connected.

The reconnected bond A-B (stored in element A) is said to be working properly when the following four test pass:

1. The pointer to element B is assigned on bond A-B.
2. The corresponding bond B-A exists on element B.
3. A pointer to element A exists in this bond B-A.
4. The element A which is being pointed to is the same element A where you started.

A useful tool disconnecting and reconnecting bonds is that each element is assigned a unique number so that elements are easily identified.

652 **Acknowledgments**

653 = enter acknowledgments here =

654 References

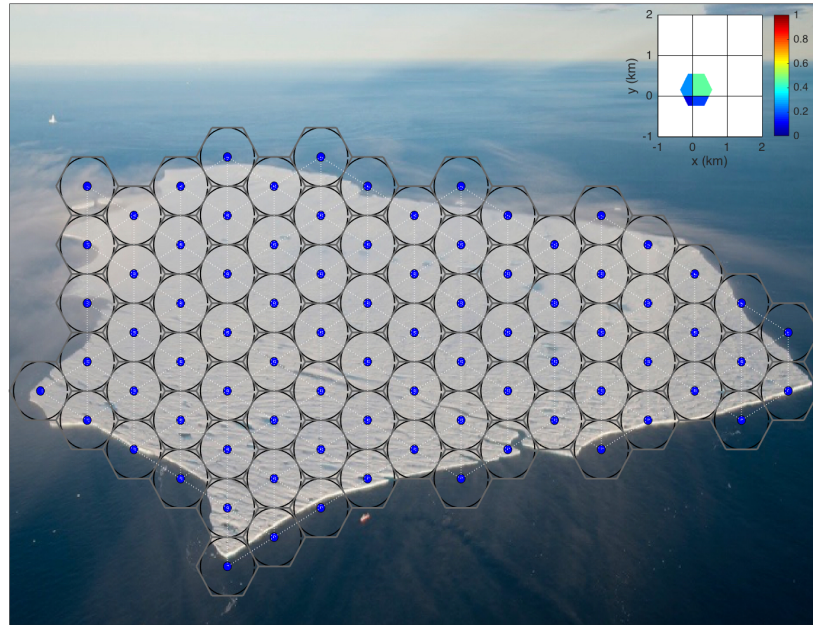
- 655 Asay-Davis, X. S., S. L. Cornford, B. K. Galton-Fenzi, R. M. Gladstone, G. H. Gud-
 656 mundsson, D. M. Holland, P. R. Holland, and D. F. Martin (2016), Experimental de-
 657 sign for three interrelated marine ice sheet and ocean model intercomparison projects:
 658 MISMIP v. 3 (MISMIP+), ISOMIP v. 2 (ISOMIP+) and MISOMIP v. 1 (MISOMIP1).
 659 *Geoscientific Model Development* 9, no. 7: 2471.
- 660 Arrigo, K. R., G. L. van Dijken, D. G. Ainley, M. A. Fahnestock, and T. Markus (2002).
 661 Ecological impact of a large Antarctic iceberg. *Geophys. Res. Lett.*, 29(7).
- 662 Alley, R. B., H. J. Horgan, I. Joughin, K. M. Cuffey, T. K. Dupont, B. R. Parizek, S.
 663 Anandakrishnan, and J. Bassis (2008), A simple law for ice-shelf calving. *Science* 322,
 664 no. 5906, 1344-1344.
- 665 Bassis, J. N., and S. Jacobs (2013), Diverse calving patterns linked to glacier geometry.
 666 *Nature Geoscience*, 6(10), 833-836.
- 667 Benn, D. I., C. R. Warren, and R. H. Mottram (2007). Calving processes and the dynam-
 668 ics of calving glaciers. *Earth-Science Reviews*, 82(3), 143-179.
- 669 Bigg, G. R., Wadley, M. R., Stevens, D. P., and Johnson, J. A. (1997), Modeling the dy-
 670 namics and thermodynamics of icebergs. *Cold Regions Science and Technology*, 26(2),
 671 113-135.
- 672 Borstad, C. P., A. Khazendar, E. Larour, M. Morlighem, E. Rignot, M. P. Schodlok, and
 673 H. Seroussi (2012), A damage mechanics assessment of the Larsen B ice shelf prior to
 674 collapse: Toward a physically-based calving law, *Geophys. Res. Lett.*, 39, L18502
- 675 Biddle, L. C., J. Kaiser, K. J. Heywood, A. F. Thompson and A. Jenkins (2015), Ocean
 676 glider observations of iceberg-enhanced biological productivity in the northwestern
 677 Weddell Sea, *Geophys. Res. Lett.*, 42, 459-465.
- 678 De Rydt, J., and G. H. Gudmundsson (2016), Coupled ice shelf ocean modeling and com-
 679 plex grounding line retreat from a seabed ridge. *J. of Geophys. Res.: Earth Surface*,
 680 121(5), 865-880.
- 681 Dunne, J.P., J.G. John,, A.J. Adcroft, S.M. Griffies, R.W. Hallberg, E. Shevliakova, R.J.
 682 Stouffer, W. Cooke, K.A. Dunne, M.J Harrison, and J.P. Krasting (2012), GFDL's
 683 ESM2 global coupled climate-carbon Earth System Models. Part I: Physical formula-
 684 tion and baseline simulation characteristics. *J. of Climate*, 25(19), 6646-6665.
- 685 Depoorter, M. A., J. L. Bamber, J. A. Griggs, J. T. M. Lenaerts, Stefan RM Ligtenberg,
 686 M. R. van den Broek, and G. Moholdt (2013), Calving fluxes and basal melt rates of
 687 Antarctic ice shelves. *Nature*, 502(7469), 89-92.
- 688 Determan J., Gerdes R. (1994), Melting and freezing beneath ice shelves: implications
 689 from a three-dimensional ocean-circulation model. *Ann. Glaciol.*, 20, 413-419.
- 690 Dowdeswell, J. A., and J. L. Bamber (2007), Keel depths of modern Antarctic icebergs
 691 and implications for sea-floor scouring in the geological record. *Marine Geology*,
 692 243(1), 120-131.
- 693 Duprat, L. P., G. R. Bigg, and D. J. Wilton (2016), Enhanced Southern Ocean marine pro-
 694 ductivity due to fertilization by giant icebergs. *Nature Geoscience*.
- 695 Eckert, E. R. G. (1950). Introduction to the Transfer of Heat and Mass. McGraw-Hill.
- 696 Fogwill, C.J., E. van Sebille, E.A. Cougnon, C.S. Turney, S.R. Rintoul, B.K. Galton-Fenzi,
 697 G.F. Clark, E.M. Marzinelli, E.B. Rainsley, and L. Carter (2016), Brief communication:
 698 Impacts of a developing polynya off Commonwealth Bay, East Antarctica, triggered by
 699 grounding of iceberg B09B. *The Cryosphere*, 10(6), p.2603.
- 700 Gladstone, R. M., G. R. Bigg, and K. W. Nicholls. (2001), Iceberg trajectory model-
 701 ing and meltwater injection in the Southern Ocean (1978-2012). *J. of Geophys. Res.:*
 702 *Oceans*, 106(C9), 19903-19915.
- 703 Goldberg, D. N., C. M. Little, O. V. Sergienko, A. Gnanadesikan, R. Hallberg, and M.
 704 Oppenheimer (2012), Investigation of land ice/ocean interaction with a fully coupled
 705 ice-ocean model: 1. Model description and behavior. *J. of Geophys. Res.: Earth Surface*,
 706 117(F2).

- 707 Gladish, C. V., D. M. Holland, P. R. Holland, and S. F. Price (2012), Ice-shelf basal chan-
708 nels in a coupled ice/ocean model. *J. of Glaciol.*, 58(212), 1227-1244.
- 709 Grosfeld K., R. Gerdes, J. Determan (1997), Thermohaline circulation and interaction
710 between ice shelf cavities and the adjacent open ocean. *J. Phys. Oceanogr.*, **102**, C7,
711 15959-15610.
- 712 Grosfeld, K., and H. SandhŁger, (2004). The evolution of a coupled ice shelfDocean sys-
713 tem under different climate states. *Global and Planetary Change*, 42(1), 107-132.
- 714 Hallberg, R., A. Adcroft, J. P. Dunne, J. P., Krasting, R. J., and Stouffer (2013), Sensitiv-
715 ity of twenty-first-century global-mean steric sea level rise to ocean model formulation.
716 *J. of Climate*, 26(9), 2947-2956.
- 717 Holland D. M., Jenkins A. (2001), Adaptation of an isopycnic coordinate ocean model for
718 the study of circulation beneath ice shelves. *Mon. Wea. Rev.*, 129, 1905-1927.
- 719 Holland P. R. and D. L. Feltham (2006), The effects of rotation and ice shelf topography
720 on frazil-laden Ice Shelf Water plumes. *J. Phys. Oceanogr.*, 36, 2312-2327.
- 721 Holland, D. M., and A. Jenkins (1999), Modeling thermodynamic ice-ocean interactions at
722 the base of an ice shelf. *J. of Phys. Oceanogr.* 29.8, 1787-1800.
- 723 Hellmer H.H., Olbers D. J. (1989), A two-dimensional model for the thermohaline circula-
724 tion under an ice shelf. *Antarctic Science*, 1, 325- 336.
- 725 Henderson J., J. S. P. Loe (2016), The Prospects andChallenges for Arctic Oil Develop-
726 ment. *Oil, Gas and Energy Law Journal (OGEL)*, 14 (2)
- 727 Hopkins, M. A. (1996). On the mesoscale interaction of lead ice and floes. *J. of Geophys.*
728 *Res.: Oceans*, 101(C8), 18315-18326.
- 729 Gaskill, H. S., and J. Rochester (1984). A new technique for iceberg drift prediction. *Cold*
730 *Reg. Sci. Technol.*, 8(3), 223-234.
- 731 Jakobsen, T. (2001). Advanced character physics. *In Game Developers Conference*, Vol. 3.
- 732 Jenkins, A., P. Dutrieux, S. S. Jacobs, S. D. McPhail, J. R. Perrett, A. T. Webb, and D.
733 White (2010), Observations beneath Pine Island Glacier in West Antarctica and implica-
734 tions for its retreat. *it Nature Geo.*, 3(7), 468-472.
- 735 Jacobs, S. S., A. Jenkins, C. F. Giulivi, and P. Dutrieux (2011). Stronger ocean circulation
736 and increased melting under Pine Island Glacier ice shelf. *Nature Geo.*, 4(8), 519-523.
- 737 Jongma, J. I., E. Driesschaert, T. Fichefet, H. Goosse, and H. Renssen (2009), The ef-
738 fect of dynamic-thermodynamic icebergs on the Southern Ocean climate in a three-
739 dimensional model, *Ocean Modell.*, 26, 104Ð113.
- 740 Kubat I., M. Sayed, S. Savage, T. Carrières (2005), An operational model of iceberg drift
741 *Int. J. Off. Polar Eng.*, 15 (2), 125Ð131
- 742 Lewis E.L. and R.G. Perkin (1986), Ice pumps and their rates. *J. of Geophys. Res.*, 91,
743 11756-11762.
- 744 Losch, M. (2008). Modeling ice shelf cavities in a z coordinate ocean general circulation
745 model. *J. of Geophys. Res.: Oceans*, 113(C8).
- 746 Li, B., H. Li, Y. Liu, A. Wang and S. Ji (2014), A modified discrete element model for
747 sea ice dynamics. *Acta Oceanologica Sinica*, 33(1), 56-63.
- 748 Liu, M. B. and G. R. Liu (2010), Smoothed particle hydrodynamics (SPH): an overview
749 and recent developments. *Archives of computational methods in engineering*, 17(1), 25-
750 76.
- 751 Lichéy, C., and H. H. Hellmer (2001). Modeling giant-iceberg drift under the influence of
752 sea ice in the Weddell Sea, Antarctica. *J. of Glaciol.*, 47(158), 452-460.
- 753 Levermann, A., T. Albrecht, R. Winkelmann, M. A. Martin, M. Haseloff, and I. Joughin.
754 (2012), Kinematic first-order calving law implies potential for abrupt ice-shelf retreat.
755 *The Cryosphere*, 6(2), 273-286.
- 756 Mountain, D. G. (1980). On predicting iceberg drift. *Cold Reg. Sci. Technol.*, 1(3-4), 273-
757 282.
- 758 Martin, T., and Adcroft, A. (2010), Parameterizing the fresh-water flux from land ice to
759 ocean with interactive icebergs in a coupled climate model. *Ocean Modelling*, 34(3),

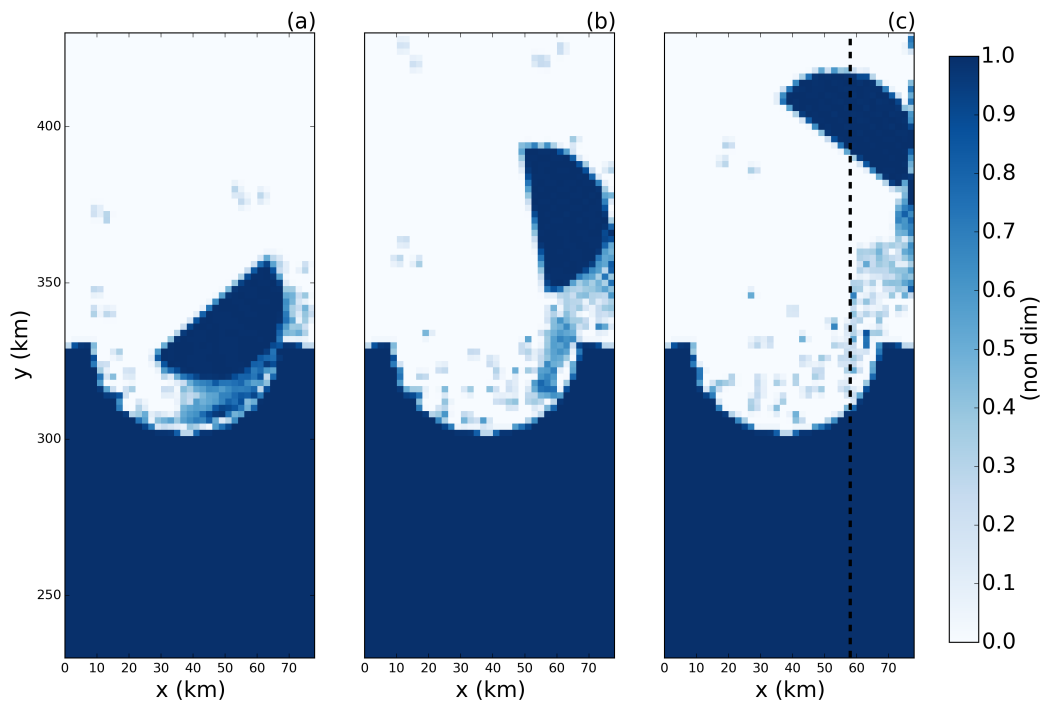
- 760 111-124.
- 761 Marsh, R., V. O. Ivchenko, N. Skliris, S. Alderson, G. R. Bigg, G. Madec, A. T. Blaker
 762 Y. Aksenov, B. Sinha, A.C. Coward, and J.L. Sommer (2015), NEMO δ ICB (v1. 0):
 763 interactive icebergs in the NEMO ocean model globally configured at eddy-permitting
 764 resolution. *Geoscientific Model Development* 8, no. 5 (2015): 1547-1562.
- 765 MacAyeal D.R. (1984), Thermohaline Circulation Below the Ross Ice Shelf: A Conse-
 766 quence of Tidally Induced Vertical Mixing and Basal Melting. *J. Geophys. Res.*, 89,
 767 597-606
- 768 Merino, N., Le Sommer, J., Durand, G., Jourdain, N. C., Madec, G., Mathiot, P., and
 769 Tournadre, J. (2016), Antarctic icebergs melt over the Southern Ocean: climatology and
 770 impact on sea ice. *Ocean Modelling*, 104, 99-110.
- 771 Nicholls K.W. (1996), Temperature variability beneath Ronne Ice Shelf, Antarctica, from
 772 thermistor cables. *J. Phys. Oceanogr.*, 11, 1199-1210.
- 773 Nicholls KW, Østerhus S, Makinson K (2009), Ice-Ocean processes over the continental
 774 shelf of the southern Weddell Sea, Antarctica: a review. *Rev. Geophys.* 47(3).
- 775 Omelyan, I. P., M. I. Mryglod, and R. Folk (2002), Optimized Verlet-like algorithms for
 776 molecular dynamics simulations. *Physical Review E*, 65(5), 056706.
- 777 Rignot, E., S. Jacobs, J. Mouginot, and B. Scheuchl (2013), Ice-shelf melting around
 778 Antarctica. *Science*, 341, no. 6143 (2013): 266-270.
- 779 Robinson, N. J., M. J. M. Williams, P. J. Barrett, and A. R. Pyne (2010), Observations of
 780 flow and ice-ocean interaction beneath the McMurdo Ice Shelf, Antarctica, *J. Geophys.*
 781 Res., 115, C03025
- 782 Pizzolato, L., S. E. Howell, C. Derksen, J. Dawson, L. Copland (2014), Changing sea ice
 783 conditions and marine transportation activity in Canadian Arctic waters between 1990
 784 and 2012, *Climatic Change* 123 (2), 161173.
- 785 Pan, W., A. M. Tartakovsky, and J. J. Monaghan (2013). Smoothed particle hydrodynam-
 786 ics non-Newtonian model for ice-sheet and ice-shelf dynamics. *J. of Comp. Phys.*, 242,
 787 828-842.
- 788 Pralong, A., and M. Funk (2005), Dynamic damage model of crevasse opening and appli-
 789 cation to glacier calving, *J. Geophys. Res.*, 110, B01309.
- 790 Sergienko, O. V. (2013). Basal channels on ice shelves. *J. of Geophys. Res.: Earth Surface*,
 791 118(3), 1342-1355.
- 792 Silva, T. A. M., Bigg, G. R., and Nicholls, K. W. (2006), Contribution of giant icebergs to
 793 the Southern Ocean freshwater flux. *J. of Geophys. Res.: Oceans*, 111(C3).
- 794 Smith, K., B. Robison, J. Helly, R. Kaufmann, H. Ruhl, H., T. Shaw, and M. Vernet
 795 (2007), Free-drifting icebergs: Hotspots of chemical and biological enrichment in the
 796 Weddell Sea, *Science*, 317, 478-482.
- 797 Shepherd, A., and D. Wingham (2007). Recent sea-level contributions of the Antarctic and
 798 Greenland ice sheets. *Science*, 315(5818), 1529-1532.
- 799 Stern, A. A., D. M. Holland, P. R. Holland, A. Jenkins and J. Sommeria (2014), The ef-
 800 fect of geometry on ice shelf ocean cavity ventilation: a laboratory experiment. *Experi-*
 801 *ments in Fluids*, 55(5), 1-19.
- 802 Stern, A.A., Johnson, E., Holland, D.M., Wagner, T.J., Wadhams, P., Bates, R., Abraham-
 803 sen, E.P., Nicholls, K.W., Crawford, A., Gagnon, J. and Tremblay, J.E. (2015), Wind-
 804 driven upwelling around grounded tabular icebergs. *J. of Geophys. Res.: Oceans*, 120(8),
 805 5820-5835.
- 806 Stern, A. A., A. Adcroft, and O. Sergienko (2016), The effects of Antarctic iceberg calv-
 807 ing size distribution in a global climate model. *J. of Geophys. Res.: Oceans*, 121(8),
 808 5773-5788.
- 809 Swope, W. C., H. C. Andersen, P. H. Berens, and K. R. Wilson (1982), A computer sim-
 810 ulation method for the calculation of equilibrium constants for the formation of physi-
 811 cal clusters of molecules: Application to small water clusters. *The Journal of Chemical*
 812 *Physics* 76, no. 1, 637-649.

- 813 Tournadre, J., N. Bouhier, F. Girard-Ardhuin, and F. RÖmy (2016), Antarctic icebergs dis-
814 tributions 1992-2014. *J. Geophys Res: Oceans*.
- 815 Turnbull I.D., N. Fournier, M. Stolwijk, T. Fosnaes, D. McGonigal (2015), Operational
816 iceberg drift forecasting in Northwest Greenland, *Cold Reg. Sci. Technol.* 110, 1-18
- 817 Unger, J. D., 2014. Regulating the Arctic Gold Rush: Recommended Regulatory Reforms
818 to Protect Alaska's Arctic Environment from Offshore Oil Drilling Pollution . *Alaska L.*
819 *Rev*, 31
- 820 Vernet, M., et al. (2012), Islands of ice: Influence of free-drifting Antarctic icebergs on
821 pelagic marine ecosystems, *Oceanography*, 25(3), 38Ð39
- 822 Wagner, T. J., Wadhams, P., Bates, R., Elosegui, P., Stern, A., Vella, D., E. P. Abraham-
823 sen, A. Crawford, and Nicholls, K. W. (2014), The ÒfootlooseÓ mechanism: Iceberg
824 decay from hydrostatic stresses. *Geophys. Res. Lett.*, 41(15), 5522-5529.
- 825 Weeks, W. F., and W. J. Campbell (1973). Icebergs as a fresh-water source: an appraisal.
826 *J. of Glaciol.*, 12(65), 207-233.
- 827 White, L., A. Adcroft, and R. Hallberg (2009), High-order regridding-remapping schemes
828 for continuous isopycnal and generalized coordinates in ocean models. *J. of Comp.*
829 *Phys.*, 228(23), 8665-8692.

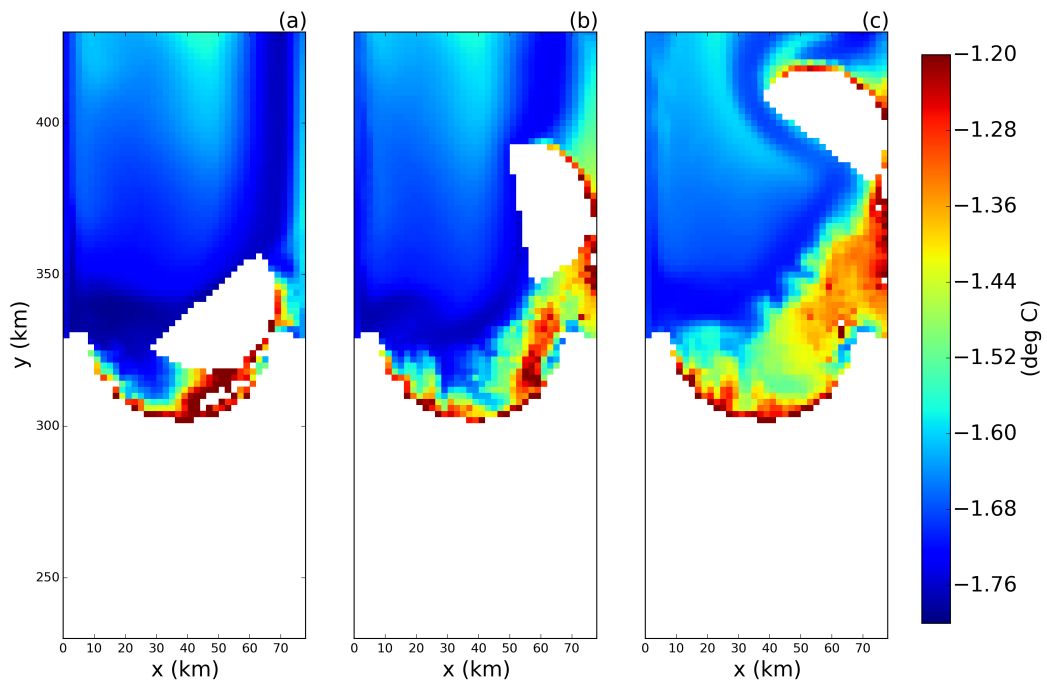
Parameter	Symbol	Value	Unit
Domain Length	L_x	80	km
Domain Width	L_y	480	km
Horizontal Resolution	Δx	2	km
Number of vertical layers	N_l	72	non-dim
Horizontal Viscosity	ν_H	6.0	$\frac{m^2}{s}$
Diapycnal Viscosity	ν_V	10^{-3}	$\frac{m}{s}$
Horizontal Diffusivity	ϵ_H	1.0	$\frac{m^2}{s}$
Diapycnal Diffusivity	ϵ_V	5×10^{-5}	$\frac{m^2}{s}$
Initial Surface Temperature	T_t	-1.9	°C
Initial Bottom Temperature	T_b	1.0	°C
Initial Surface Salinity	S_t	33.8	psu
Initial Bottom Salinity	S_b	34.7	psu
Maximum Ocean depth	H_{ocean}	720	m
Relaxation Time of Sponge Layer	T_{sponge}	0.1	days
Time Step for Static Shelf Experiment	dt_{Static}	1000	s
Time Step for Iceberg Calving Experiment	$dt_{Calving}$	10	s



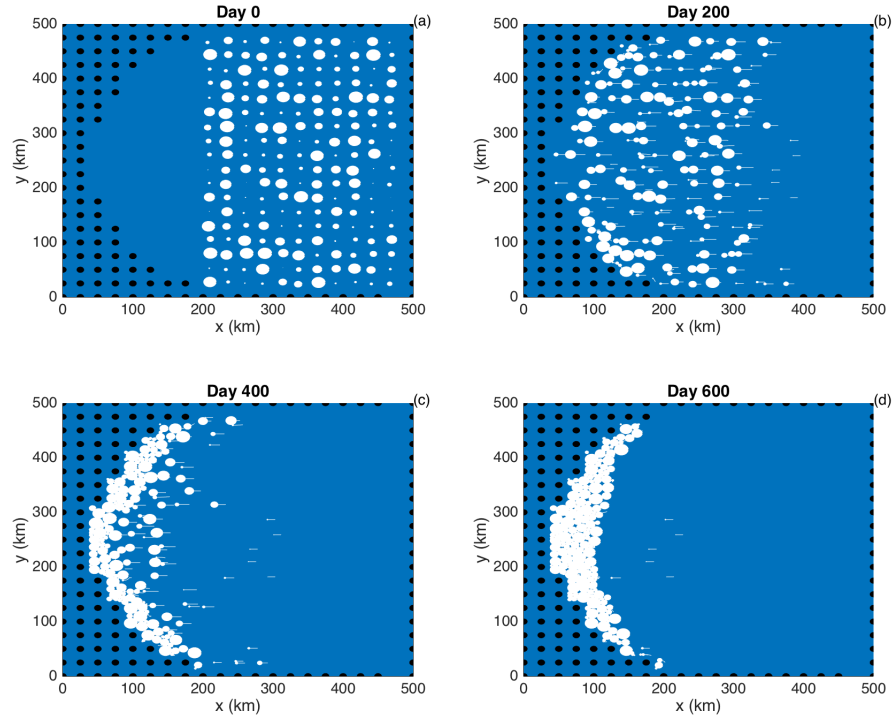
830 **Figure 1.** Schematic showing how Lagrangian elements are used when modeling tabular icebergs. La-
 831 grangian elements (blue dots) are initialized in a staggered lattice covering the surface area of the iceberg.
 832 For purposes of mass aggregation, the ice elements are assumed to have hexagonal shape (grey hexagons).
 833 For purposes of element interactions, the ice elements are assumed to be circular (black circles). Elements
 834 are initially bonded to adjacent elements using numerical bonds (dashed white lines). These numerical bonds
 835 form equilateral triangles which give the shape rigidity. The inset panel shows a schematic of the intersection
 836 of a hexagonal element and the ocean grid. The colors indicate the fraction of the hexagon that lies in each
 837 grid cell. These fractions are used as weights to spread LBIM properties to the ocean grid (see text for more
 838 details) The background photo in the larger schematic is an areal photograph of iceberg PIIB (Area= 42 km²)
 839 taken in Baffin Bay in 2012. The red ship can be identified on the bottom of the photo for scale.



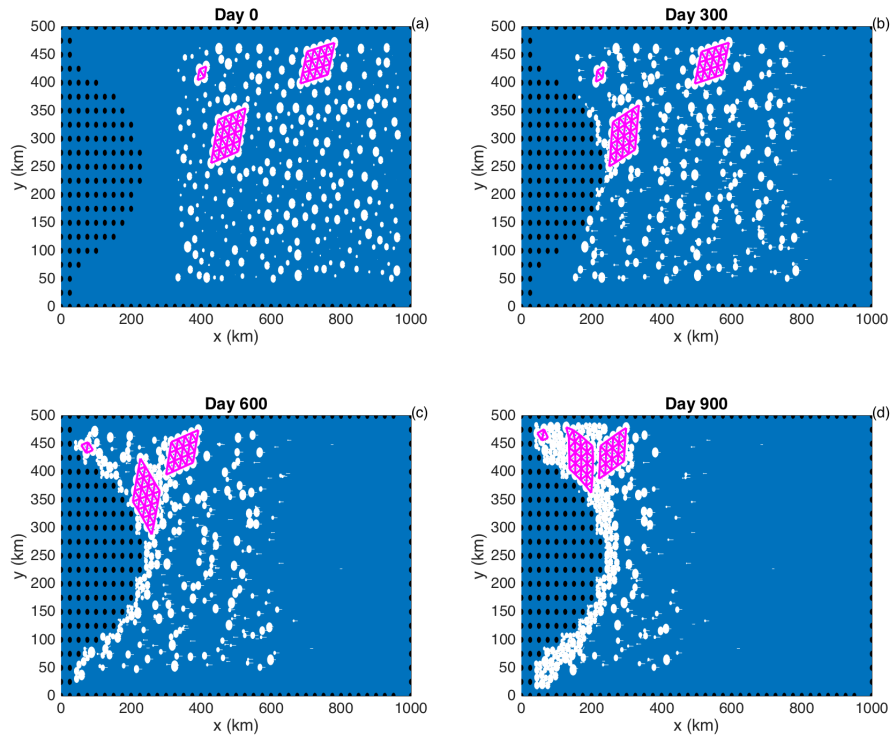
840 **Figure 2.** Snapshots of the fraction of ice cover in the LBIM tabular iceberg calving simulation. Snapshots
841 are taken (a) 7, (b) 15, and (c) 30 days after calving. The dashed line in panel (c) shows the location of the
842 vertical transects shown in Figures 7 and 8.



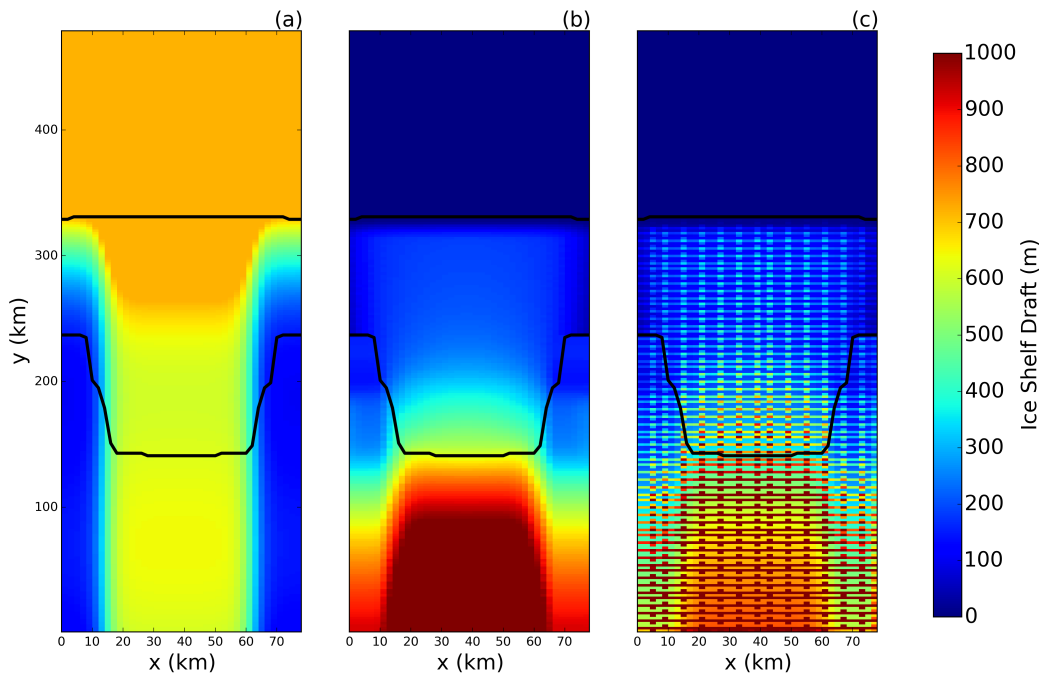
843 **Figure 3.** Snapshots of the sea surface temperature in the LBIM tabular iceberg calving simulation. Snap-
844 shots are taken (a) 7, (b) 15, and (c) 30 days after calving. Regions with ice area fraction = 1 area plotted in
845 white.



846 **Figure 4.** Results of an ice-only LBIM simulation with no bonds between ice elements.
 847 Ice elements are initialized throughout the domain, as shown in panel (a). The elements are forced by an imposed westward
 848 ocean current of $u=0.1\text{m/s}$ (no ocean model is used). Forces due to sea surface slope, atmospheric drag, Cori-
 849 olis and sea ice drag are set to zero. The figure shows snapshots of ice element positions at time (a) $t=0$, (b)
 850 200, (c) 400, (d) 600 days. The size of the dots shows the surface area (and interaction diameter) of each ice
 851 element. The white tails behind the elements show the elements' positions over the preceding two days. Land
 852 points are shown by black circles.



853 **Figure 5.** Results of an ice-only LBIM simulation using bonds between elements. Ice elements are ini-
 854 tialized throughout the domain, as shown in panel (a). Three tabular icebergs are included, with 25, 16 and 4
 855 elements respectively. The elements are forced by an imposed westward ocean current of $u=0.1\text{m/s}$ (no ocean
 856 model is used). Forces due to sea surface slope, atmospheric drag, Coriolis and sea ice drag are set to zero.
 857 The figure shows snapshots of ice element positions at time (a) $t=0$, (b) 300, (c) 600, (d) 900 days. The size
 858 of the dots shows the surface area (and interaction diameter) of each ice element. The white tails behind the
 859 elements show the elements' positions over the preceding two days. Bonds between ice elements are plotted
 860 in magenta. Land points are shown by black circles.



861 **Figure 6.** (a) Ocean bottom topography and (b) ice-shelf draft used to initialize the tabular iceberg calv-
862 ing simulation. The ice draft is calculated from the total mass in an ocean grid cell after the mass-spreading
863 interpolation has been applied (as explained in Section 2.3). (c) Initial ice draft that would be calculated if the
864 mass-spreading interpolation were not used (i.e.: elements treated as point masses).

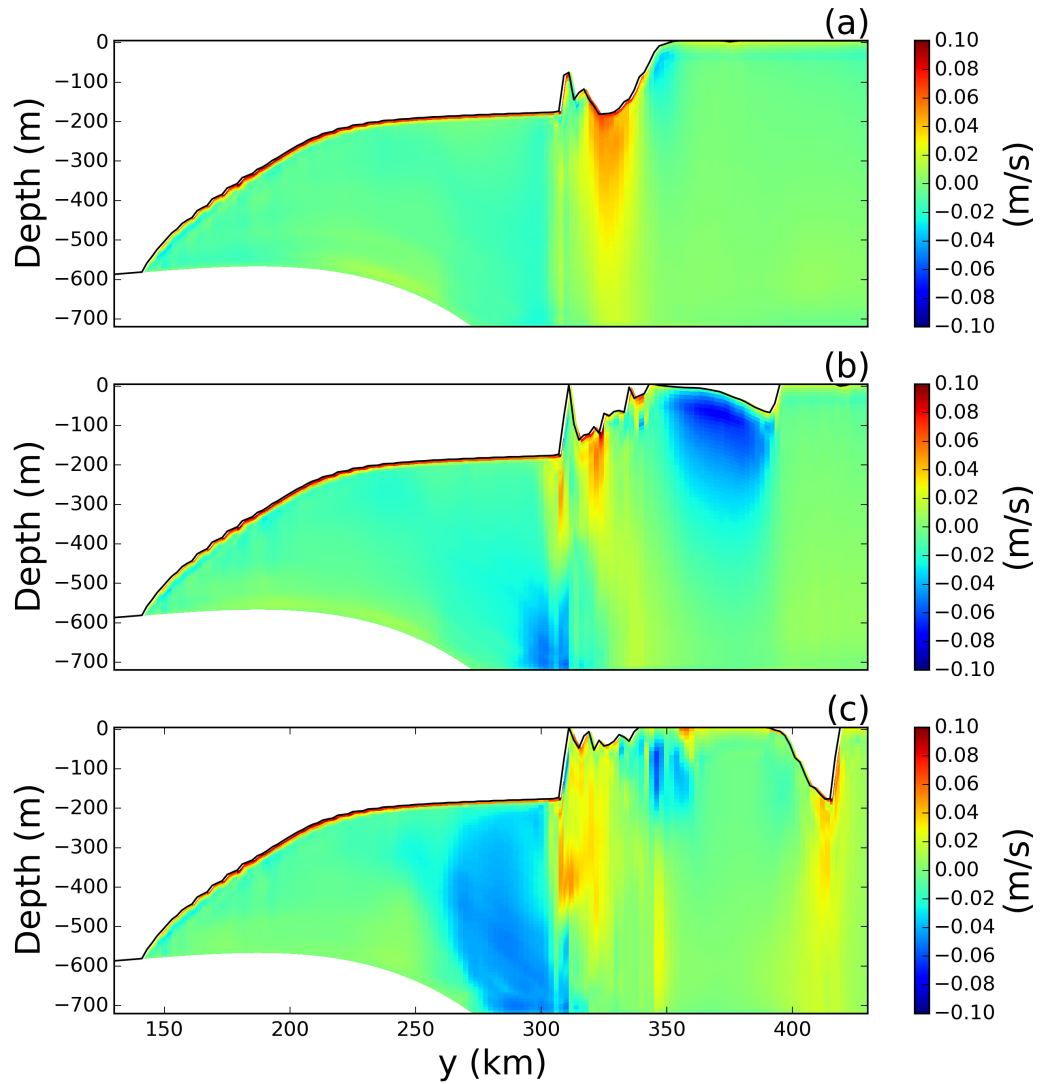
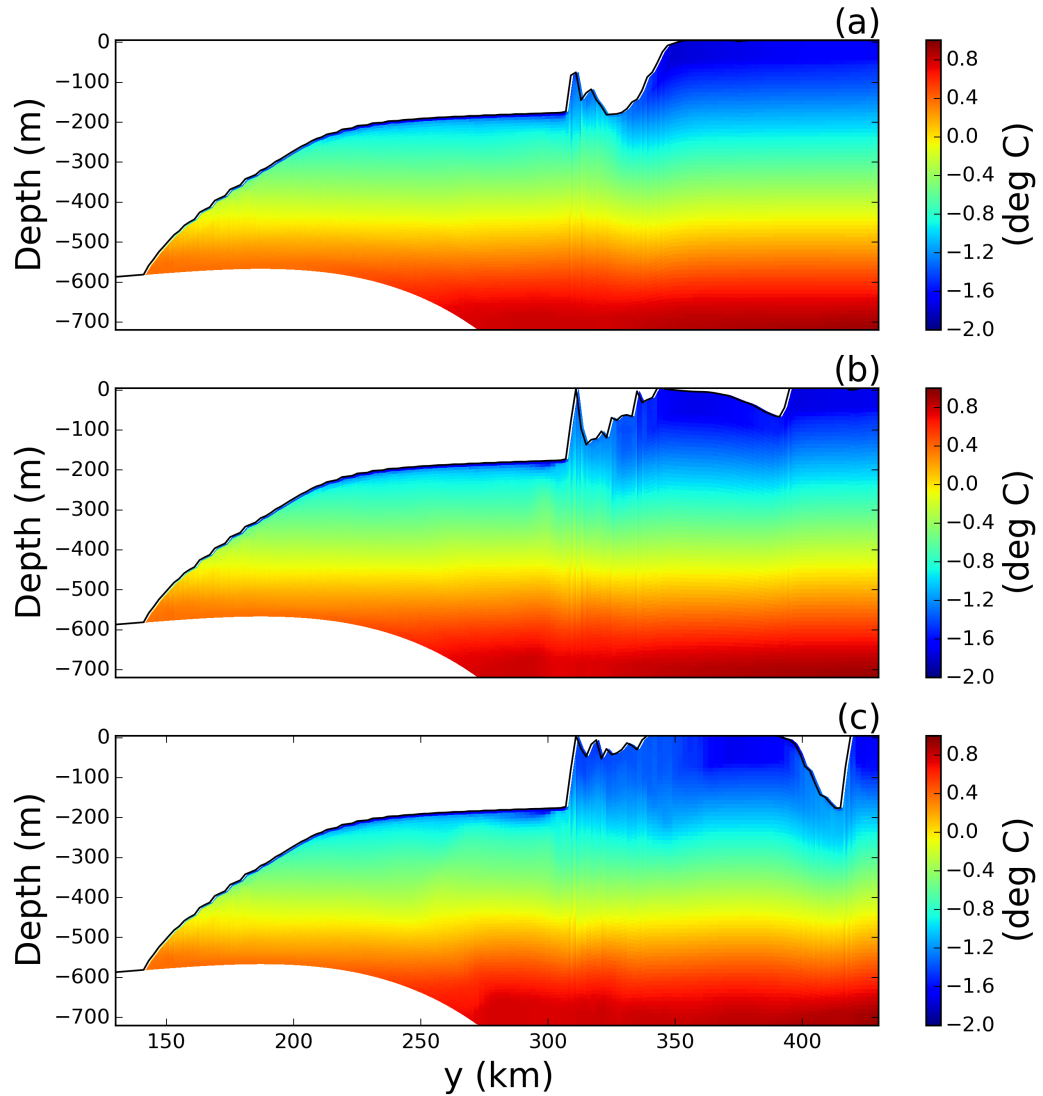
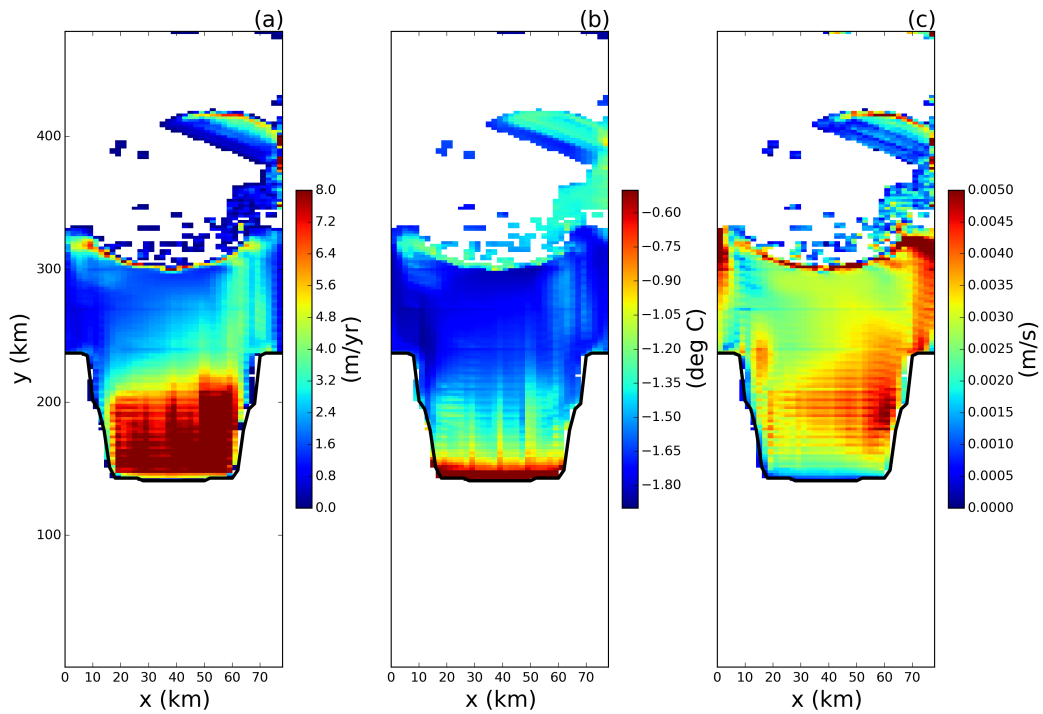


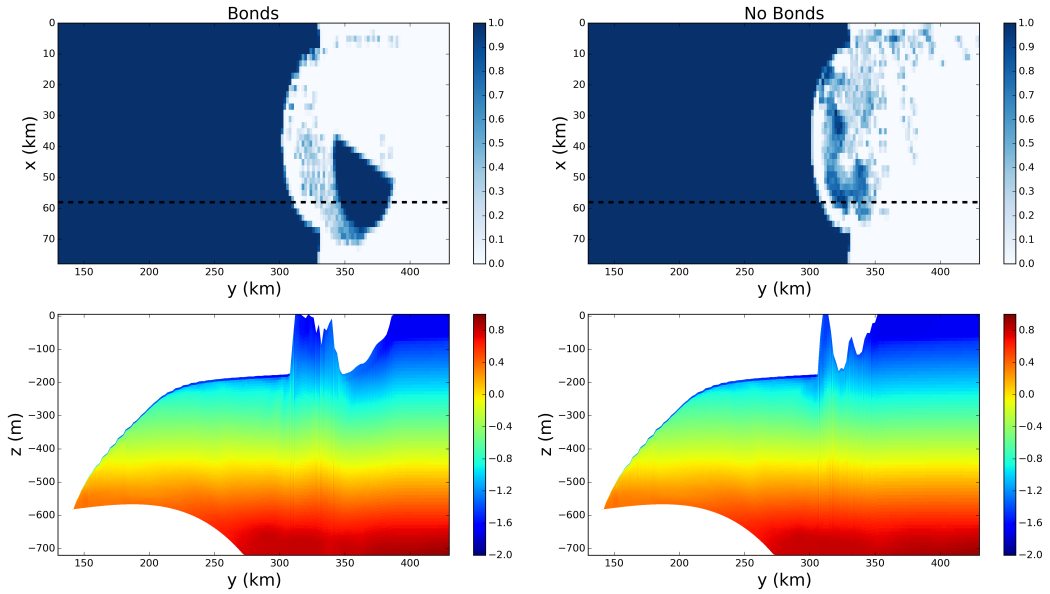
Figure 7. Snapshots of vertical sections of meridional velocity at $x = 58$ km in the LBIM tabular iceberg calving simulation. Snapshots are taken (a) 7, (b) 15, and (c) 30 days after calving. The position of the transects is shown by the dashed line in Figure 2c.



868 **Figure 8.** Snapshots of vertical sections of ocean temperature at $x = 58$ km in the LBIM tabular iceberg
 869 calving experiment. Snapshots are taken (a) 7, (b) 15, and (c) 30 days after calving. The position of the
 870 vertical transects is shown by the dashed lines in Figure 2c.



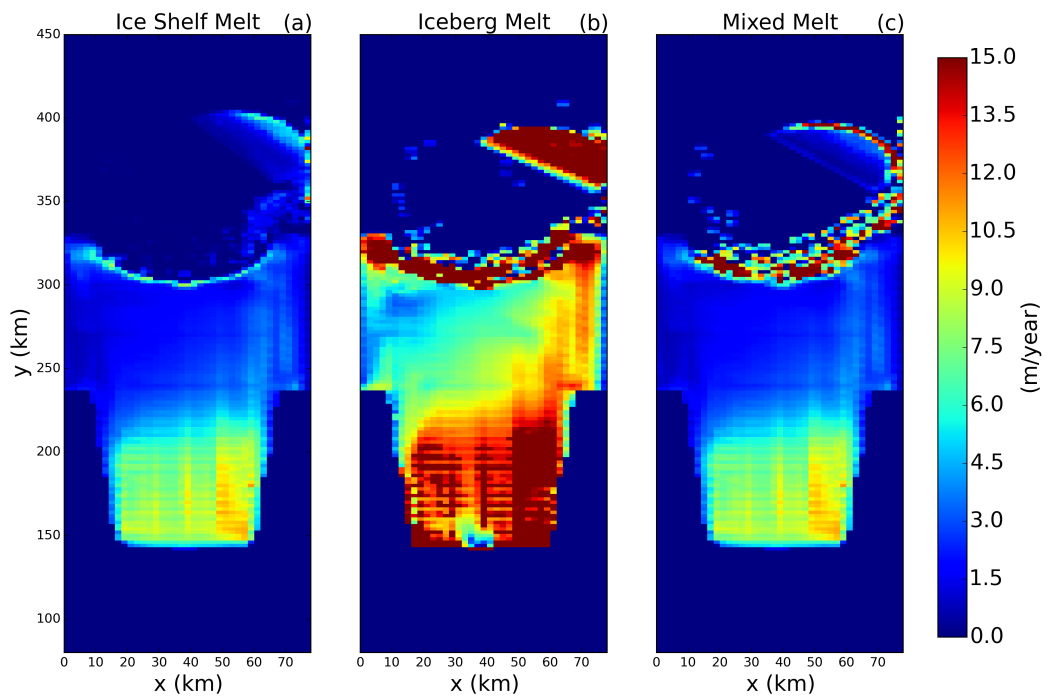
871 **Figure 9.** Results of the tabular iceberg calving simulation 30 days after the iceberg calves. The three panels
872 show snapshots of the (a) melt rate, (b) top-of-ocean temperature and (c) u^* at the base of the ice shelf.
873 Fields are only shown in regions where the ice area fraction is ≥ 0.8 .



874 **Figure 10.** Results from the tabular iceberg calving experiment with and without iceberg bonds. The top
 875 row shows the fractional ice cover for the simulations (a) with and (b) without numerical bonds. The bottom
 876 row shows the corresponding vertical temperature section at $x = 58$ km for the simulation (c) with and (d)
 877 without bonds. The location of the vertical transects in panels (c) and (d) are shown by the dashed lines in
 878 panels (a) and (b), respectively. All snapshots are taken at time $t = 30$ days. The simulations use wind stress
 879 $\vec{\tau} = <0.0, 0.05>$.

880

9 Extra Figure:



881 **Figure 11.** Melt rate 30 days after calving for simulations using (a) three equation
882 model, (b) icebergs drift parametrization, (c) a mixture between the two (as described in Section 2.5.)

883 **10 Supplementary Material**

884 The experiment configuration used to initialize the calving tabular iceberg simulation
885 (in this study) is the same as that of the Ocean0 setup in the MISOMIP, with the follow-
886 ing three changes made:

- 887 1. The ‘calving criteria’ used in the MISOMIP study (which states that all points in
888 the ice shelf with thickness less than 100m are set to zero thickness) has not been
889 used.
- 890 2. The ice shelf has been thickened on the flanks of the domain, so that the latitude of
891 the grounding line increases away from the center of the ice shelf.
- 892 3. The ice shelf is configured to be symmetric about its meridional center line ($x =$
893 $\frac{L_x}{2}$). This was achieved by using the average of the left and right flanks of the ice-
894 shelf thickness.

895 These three changes were made in order to make the circulation beneath the ice shelf eas-
896 ier to interpret.